Editors' Suggestion

Programmable Quantum Annealing Architectures with Ising Quantum Wires

Xingze Qiu,[1] Peter Zoller,[2,3] and Xiaopeng Li[1,4,*]

[1] *State Key Laboratory of Surface Physics, Institute of Nanoelectronics and Quantum Computing, and Department of Physics, Fudan University, Shanghai 200433, China*

[2] *Center for Quantum Physics, University of Innsbruck, Innsbruck 6020, Austria*

[3] *Institute for Quantum Optics and Quantum Information of the Austrian Academy of Sciences, Innsbruck 6020, Austria*

[4] *Shanghai Qi Zhi Institute, AI Tower, Xuhui District, Shanghai 200232, China*

(Received 1 August 2020; accepted 16 October 2020; published 6 November 2020)

Quantum annealing aims at solving optimization problems efficiently by preparing the ground state of an Ising spin-Hamiltonian quantum mechanically. A prerequisite of building a quantum annealer is the implementation of programmable long-range two-, three-, or multispin Ising interactions. We discuss an architecture, where the required spin interactions are implemented via two-port or in general multi-port quantum Ising wires connecting the spins of interest. This quantum annealing architecture of spins connected by Ising quantum wires can be realized by exploiting the three-dimensional (3D) character of atomic platforms, including atoms in optical lattices and Rydberg tweezer arrays. The realization only requires engineering on-site terms and two-body interactions between nearest neighboring qubits. The locally coupled spin model on a 3D cubic lattice is sufficient to effectively produce arbitrary all-to-all coupled Ising Hamiltonians. We illustrate the approach for few-spin devices solving Max-Cut and prime factorization problems, and discuss the potential scaling to large atom-based systems.

DOI: 10.1103/PRXQuantum.1.020311

I. INTRODUCTION

There has been growing research interest in quantum annealing in an effort to speed up complex search and optimization problems [1–3], including bounded-error quantum polynomial-time (BQP), NP-complete, and NP-hard problems [1,4]. While a quantum annealer might not reduce the classical computation complexity of NP-hard problems $O(\exp[\alpha N^{\gamma}])$ (with N the problem size) to polynomial [5–9], an exponential speedup for BQP has been suggested [10,11], and one might gain significant improvement on coefficients α and γ for NP problems [1,4,12] compared to classical algorithms. Because of important implications for both science [4] and commercial applications [13], quantum annealing has received significant attention in recent years [12,14–18].

Among various platforms considered for building a quantum annealer [19,20], cold atoms trapped in an optical potential provide a scalable quantum simulation platform with versatile controllability [21], as demonstrated in experiments emulating high-temperature superconductivity, quantum phase transitions and criticality, and quantum thermalization with atomic Hubbard models with tens to thousands of atoms [21]. Recent experiments have achieved single-site control and free programmability in optical lattices [22–27], and similar optical tweezer arrays provide us with large-spacing optical lattices with engineered spin-spin interactions through Rydberg dressing [28–32]. Thus, present atomic setups of engineered many-body systems provide us with new opportunities to build a quantum annealer.

In mapping optimization problems to a quantum annealer, however, all-to-all long-range couplings generically arise, which, for example, in atomic Hubbard models with optical lattices cannot be directly engineered. One way to approach the problem of long-range interactions is to develop spin encodings in an enlarged spin space, where programmable long-range interactions are mapped to the experimentally simpler problem of controlled local fields [15]. This comes with the requirement, however, of implementing local four-body constraints, which can be resolved in terms of two-body interactions as discussed in Ref. [17]. In contrast, in the following we discuss a completely distinctive scheme—a three-dimensional (3D) architecture for quantum annealing (Fig. 1), in which distant spins (or qubits) are coupled through an Ising ferromagnetic quantum wire playing the role of a connector mediating the

*xiaopeng_li@fudan.edu.cn

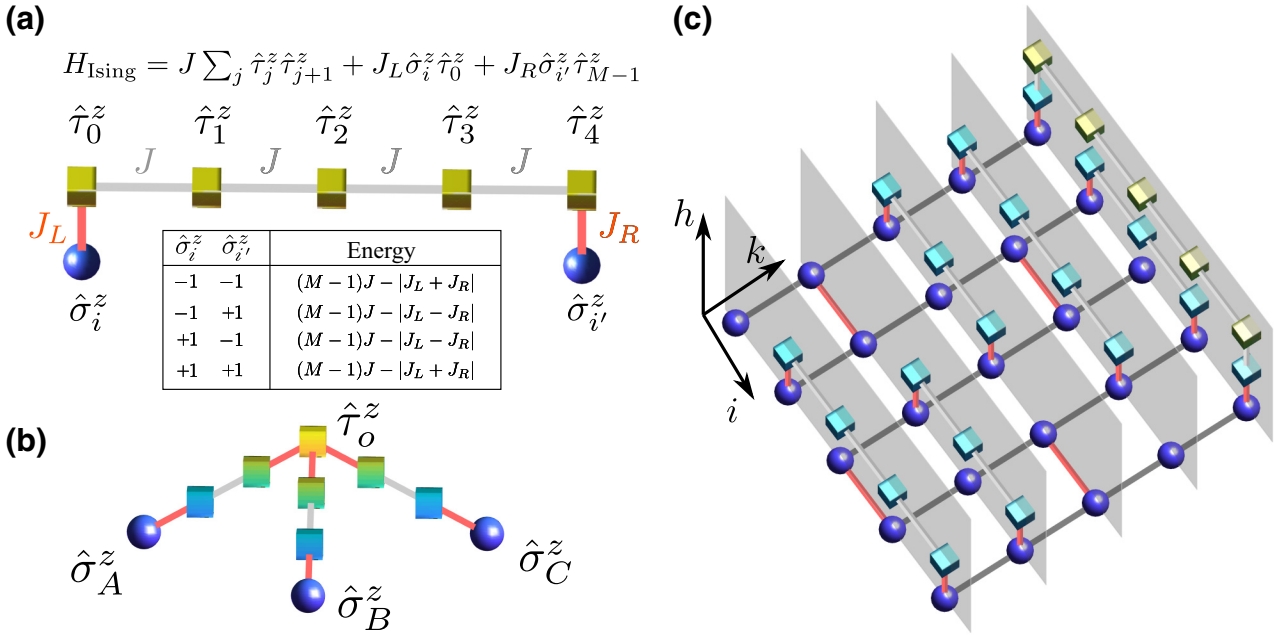

FIG. 1. Illustration of the three-dimensional cubic architecture for quantum annealing. (a) The Ising ferromagnetic quantum-wire-induced interaction, with a ferromagnetic quantum wire coupling to qubits $\hat{\sigma}_i^z$ and $\hat{\sigma}_{i'}^z$ at the two ends. The auxiliary spins in the wire are denoted as $\hat{\tau}_{j=0,1,\ldots,M-1}^z$ (the number of ancilla M is five in this example), which are ferromagnetically coupled by $J < 0$, with an Ising Hamiltonian. The coupling between $\hat{\tau}_0^z$ ($\hat{\tau}_{M-1}^z$) and $\hat{\sigma}_i^z$ ($\hat{\sigma}_{i'}^z$) is J_L (J_R). The ground state energy of the quantum wire with the two distant qubits restricted to an eigenstate subspace of $\hat{\sigma}_i^z$ and $\hat{\sigma}_{i'}^z$ is listed in the table, which determines the induced effective interaction between the two qubits. (b) The Y-junction connector for engineering a three-body interaction. With three quantum wires forming a Y junction that couples $\hat{\sigma}_{A,B,C}^z$ through $\hat{\tau}_o^z$ [Eq. (10)], an effective three-body interaction is mediated (see the main text). (c) The geometry of the three-dimensional cubic quantum annealing architecture. The blue spheres represent the N duplicated copies of logical qubits. The cubes represent the introduced ancilla. The light and dark grey links correspond to ferromagnetic couplings with fixed strengths J and J_d. The red links correspond to the programmable Ising couplings [Eq. (8)]. All couplings in this quantum annealing architecture are local and at most between two neighboring sites, and can be embedded in a regular cubic lattice. In this example we set $N = 5$ for illustration.

interactions. The ancilla spins introduced as quantum wires are carefully organized such that the 3D quantum annealing architecture can be embedded into a regular cubic lattice with nearest neighboring interaction only. This geometric arrangement comes with the requirement to duplicate the Ising spins into multiple copies to provide ports for coupling to the wires, as illustrated in Fig. 1. As discussed below, the 3D architecture can be implemented by ground state atoms in optical lattices considering superexchange interactions, or the Rydberg-dressing-induced couplings. The latter enjoys the advantage of having larger coupling strength. The scheme of quantum wire encoding programmable long-range interactions is rather flexible and the geometry can be adapted according to physical resources in an actual experimental realization. We find reasonable scalability even in the presence of thermally activated errors, potentially existent in experiments performing large-scale quantum annealing. This work indicates that large-scale atom-based quantum annealing is accessible with near-term technology. We also provide a generalization of the quantum wire construction to a quantum network mediating m-body interactions in general. An experimental demonstration of the quantum wire mediating programmable m-body interactions does not only provide a building block of the 3D quantum annealing architecture, but also opens up novel opportunities for quantum engineering of exotic spin models and interesting quantum many-body physics.

II. QUANTUM HAMILTONIAN CONSTRUCTION

In annealing solving an optimization problem is formulated as finding the ground state of an Ising spin glass model, defined on an undirected graph $G = (V, E)$ [4]. The corresponding classical Hamiltonian is

$$H[\{s\}] = \sum_{i=0}^{N-1} b_i s_i + \sum_{(ii')\in E} K_{ii'} s_i s_{i'}, \tag{1}$$

where s_i is an Ising variable ($\pm$), i labels the vertices of the graph, and N is the number of vertices. The local field b_i and the Ising coupling $K_{ii'}$ are assumed programmable and encode the optimization problem to be

solved—for example, they depend on graph edges in graph partitioning [4].

In quantum annealing, the Ising variables are promoted to Pauli-z operators ($\hat{\sigma}^z$) acting on qubits. Here the ground state is reached following an adiabatic evolution of a time-dependent Hamiltonian of a quantum system [3]

$$\hat{H}_{\rm QA}(\tau) = -\left[1-\left(\frac{\tau}{\tau_{\rm ad}}\right)\right]\sum_i \frac{\hat{\sigma}_i^x}{2} + \left(\frac{\tau}{\tau_{\rm ad}}\right)\left[\sum_{i=0}^{N-1} b_i\hat{\sigma}_i^z + \sum_{(ii')\in E} K_{ii'}\hat{\sigma}_i^z\hat{\sigma}_{i'}^z\right] \quad (2)$$

with the time $\tau \in [0, \tau_{\rm ad}]$ and $\tau_{\rm ad}$ the total evolution time. A challenge in implementing quantum annealing arises from the requirement to physically represent programmable infinite-range interactions represented by the matrix $K_{ii'}$, while physical resources available on quantum platforms are typically restricted to (quasi-)local two-body couplings. While platforms like trapped ions [33] and Rydberg arrays [34] provide long-range interactions, the requirement of long-range interactions typically interferes with scalability of the system. Below we address this problem by introducing quantum wires to connect physical qubits in a 3D geometry, as is often available in atomic platforms.

A. Local Hamiltonian construction

We start our construction by rewriting the interaction between the Ising variables s_i in Eq. (1), and similarly in the quantum case with $s_i \to \hat{\sigma}_i^z$ in Eq. (2), as

$$K_{ii'}s_is_{i'} = \min_{n_{ii'}}\left\{-2J\sum_{(ii')\in E} n_{ii'} - \sum_{(ii')\in E} 2K_{ii'} \times \left[n_{ii'} \bmod 2 - \frac{1}{2}\right]s_is_{i'}\right\}, \quad (3)$$

where the $n_{ii'}$ are auxiliary integer-valued degrees of freedom, $n_{ii'} \geq 0$. We require that the energy penalty $|J|$ dominates over the maximal coupling ($K_{\rm max} \equiv \max\{|K_{ii'}|\}$), giving

$$J < -K_{\rm max}. \quad (4)$$

Although the coupling in Eq. (3) still appears nonlocal, it can be realized by a quantum wire connecting Ising spins i and i'. We choose an Ising ferromagnetic spin chain for the wire, and the auxiliary degrees of freedom $n_{ii'}$ correspond to the number of domain wall defects in the spin chain [Fig. 1(a)]. The mediated Ising interaction between $\hat{\sigma}_i^z$ and $\hat{\sigma}_{i'}^z$ is $(|J_{L,ii'} - J_{R,ii'}| - |J_{L,ii'} + J_{R,ii'}|)/2 = -{\rm sgn}(J_{L,ii'}J_{R,ii'})\min(|J_{L,ii'}|, |J_{R,ii'}|)$, with $J_{L,ii'}$ ($J_{R,ii'}$) the coupling between $\hat{\tau}_i^z$ ($\hat{\tau}_{i'}^z$) and the leftmost (rightmost) ancilla [Fig. 1(a)]. We then set

$$J_{L,ii'} = K_{ii'}, \qquad J_{R,ii'} = -|K_{ii'}|. \quad (5)$$

To the extent such quantum wires can be implemented in a physical platform, this achieves the required scalable and programmable long-range couplings. The above construction is reminiscent of gauge fields mediating long-range interactions in field theories—for example, long-range Coulomb interactions are mediated by fluctuating electromagnetic waves in quantum electrodynamics [35]. In general, the quantum wires connecting the two distant qubits can also be implemented with other spin models or possibly even bosons, allowing the interaction mediated by the quantum wire to be analytically calculated. Here we choose the Ising ferromagnetic spin chain for the quantum wire for simplicity. In this construction, different quantum wires connecting a pair (ii') are assumed decoupled. This poses a physical requirement on assembling these quantum wires without physical crossings.

Lining up the logical qubits $\hat{\sigma}_i^z$ from $i = 0$ to $N-1$ in space, one problem arises that it is fundamentally impossible to allocate these ancilla on a regular two-dimensional lattice with a linear size of N, for the total number of quantum wires scales as $N(N-1)/2$ and their lengths, $M_{ii'}$, are of the order of N on average—$M_{ii'} \sim d_{ii'} \equiv |i-i'| \sim N$. To resolve this problem, we duplicate each logical qubit, $\vec{\hat{\sigma}}_i$ (Pauli operators), into N copies as $\vec{\hat{\sigma}}_{ik}$ with $k \in [0, N-1]$. These duplicated qubits are ferromagnetically coupled through

$$\hat{H}_{{\rm D},i} = J_d\sum_{k=0}^{N-2}\hat{\sigma}_{i,k}^z\hat{\sigma}_{i,k+1}^z \quad (6)$$

with the coupling strength $J_d < 0$.

The qubit duplication allows us to assemble quantum wires in a three-dimensional cubic lattice without any crossing. In Fig. 1(c) we show an example with $N = 5$. The duplicated logical qubits $\vec{\hat{\sigma}}_{ik}$ are placed at $(i, k, h = 0)$. The ancilla quantum wire connecting qubits i and i' is placed in a two-dimensional vertical layer with $k = \underline{i+i'}$, where $\underline{i+i'}$ is shorthand notation for the modular summation $(i + i' \bmod N)$. The quantum wire connector Hamiltonian reads

$$\hat{H}_{{\rm QWC},ii'} = J\sum_{j=0}^{M_{ii'}-2}\hat{\tau}_{ii',j}^z\hat{\tau}_{ii',j+1}^z + [K_{ii'}\hat{\sigma}_{i,\underline{i+i'}}^z\hat{\tau}_{ii',0}^z - |K_{ii'}|\hat{\sigma}_{i',\underline{i+i'}}^z\hat{\tau}_{ii',M_{ii'}-1}^z]. \quad (7)$$

The quantum wire starts from the position $(i, k = \underline{i+i'}, h = 1)$, extends vertically first, and bends towards

the i axis at $(i, \underline{i+i'}, h = \lfloor d_{ii'}/2 \rfloor)$, then bends downward at $(i', \underline{i+i'}, \lfloor d_{ii'}/2 \rfloor)$, and reaches the end at $(i', \underline{i+i'}, 1)$. The length of the ancilla quantum wire is $M_{ii'} = d_{ii'} + 2\lfloor d_{ii'}/2 \rfloor - 1$, accordingly. The quantum wires having the same $\underline{i+i'}$ are placed in the same k layer with $k = \underline{i+i'}$ (see Fig. 1). The maximal height of the 3D quantum annealing architecture along the h direction is $h_{\max} = \lceil N/2 \rceil - 1$.

With the above construction, we reach an effective local quantum annealing Hamiltonian for universal Ising spin glass problems, given as

$$\hat{H}_{\mathrm{LQA}}(\tau) = \left[1 - \left(\frac{\tau}{\tau_{\mathrm{ad}}}\right)\right]\hat{H}_0 + \frac{\tau}{\tau_{\mathrm{ad}}}\hat{H}_P, \tag{8a}$$

$$\hat{H}_0 = -\sum_{ik}\frac{\hat{\sigma}^x_{ik}}{2} - \sum_{(ii')\in E}\sum_{j=0}^{M_{ii'}-1}\frac{\hat{\tau}^x_{ii',j}}{2}, \tag{8b}$$

$$\hat{H}_P = \sum_{i=0}^{N-1}[\hat{H}_{\mathrm{D},i} + b_i\hat{\sigma}^z_{i0}] + \sum_{(ii')\in E}\hat{H}_{\mathrm{QWC},ii'}. \tag{8c}$$

Here the local fields b_i are applied to $\hat{\sigma}^z_{ik}$ with $k = 0$ only, with an alternative way being to distribute that to all duplicated N copies. The ferromagnetic interactions J and J_d that couple the ancilla and the duplicated logical qubits have fixed strengths, i.e., independent of the indices i and k. The interactions between the ancilla and the duplicated logical qubits, $K_{ii'}$, encode the distant couplings in the Ising spin glass and are required to be programmable. We note here that the quantum wire connector Hamiltonian, $H_{\mathrm{QWC},ii'}$, should be replaced by a direct coupling $K_{ii'}\hat{\sigma}^z_{i,\underline{i+i'}}\hat{\sigma}^z_{i',\underline{i+i'}}$ for $i' = i \pm 1$. In this way, we have constructed a local 3D quantum annealer for the all-to-all coupled spin glass that is embedded in a regular 3D cubic array of qubits with nearest-neighbor interaction only. The size of this cubic lattice is $N \times N \times \lceil N/2 \rceil$. The noncrossing requirement to avoid potential engineering difficulty in experiments is satisfied.

We remark here that, given the geometrical structure of the proposed 3D cubic architecture [Fig. 1(c)], it often permits efficient compression. For example, the vertical layers not containing any quantum wires can be removed, and the height of one quantum wire can be lowered if there are no other wires below that. With the compression, for spin glass defined on a graph with its maximal degree $D_{\max}$ being finite, the total number of physical qubits in this 3D local quantum annealing architecture is proportional to N^2, having the same scaling form as in Lechner-Hauke-Zoller model [15]. For many difficult NP problems, including unit-disk graph problems [36], the most difficult instances of 3SAT [37], and partition of power-law degree distributed social networks [38], the degree $D_{\max}$ in the corresponding Ising formulation is typically a finite number. For Ising models on graphs with different connectivity, we would end up in the compression with the encoding architectures having different geometries. While this may be difficult to implement with solid-state systems [39,40], dynamical manipulation of the geometry can be achieved by controlling lasers with atomic quantum systems (see Sec. V).

One property we would like to emphasize about the 3D cubic architecture is that it has the ingredient of repetition error-correcting code due to the logical qubit duplication. This gives the quantum annealing architecture protection against readout errors. We assume an independent single-spin-flip error with probability $\epsilon < 50\%$ in the readout. Taking a majority voting scheme for decoding, the probability for the decoded logical bit configuration to be erroneous has an exponentially small upper bound,

$$p_{\mathrm{logical}} \leq N \exp\left(-ND\left[\frac{\lfloor N/2 \rfloor}{N}\middle\|(1-\epsilon)\right]\right), \tag{9}$$

with $D(a\|b)$ the standard relative entropy $a\ln(a/b) + (1-a)\ln[(1-a)/(1-b)]$. This result is obtained from the Chernoff bound for the binomial distribution of spin flips, which is reasonably tight. The 3D cubic quantum annealing architecture is thus robust against readout errors.

B. Engineering m-body interactions through a quantum wire network

Since a direct formulation of many computation problems such as 3SAT and prime factorization requires three-body [41] or higher-order interactions [10], here we generalize the quantum wire connector protocol to a quantum wire network that mediates m-body interactions in general. The application of this engineering scheme could reach beyond the present scope of quantum annealer construction, and may be adopted to programmable quantum simulations of novel quantum many-body physics.

We consider three qubits A, B, and C with the corresponding Pauli operators $\hat{\sigma}^z_A$, $\hat{\sigma}^z_B$, $\hat{\sigma}^z_C$. With an ancilla $\hat{\tau}^z_o$ introduced to connect the three qubits through three Ising ferromagnetic quantum wires [see Fig. 1(b)], we can achieve an interaction

$$H_Y = 2J_Y\hat{\tau}^z_o[\hat{\sigma}^z_C - \Delta(\hat{\sigma}^z_A + \hat{\sigma}^z_B) + (1+\Delta)] \tag{10}$$

with J_Y parameterizing the overall interaction strength and Δ a dimensionless parameter describing the energy gap to be discussed below. The connections then make a Y junction with the qubits A, B, and C placed at the three ends, and the ancilla ($\hat{\tau}^z_o$) at the middle crossing point. Assuming that $\Delta > 2$, the effective interaction mediated by the ancilla is obtained by projecting to the low-energy subspace [42] having $2\hat{\tau}^z_o = \hat{\sigma}^z_A\hat{\sigma}^z_B + \hat{\sigma}^z_A + \hat{\sigma}^z_B - 1$. The states

violating this condition have a minimal energy gap of $4(\Delta-2)J_Y$. The projection produces

$$H_{Y,\mathrm{eff}}/J_Y = \hat{\sigma}_A^z\hat{\sigma}_B^z\hat{\sigma}_C^z + (1+\Delta)(\hat{\sigma}_A^z+\hat{\sigma}_B^z) - \hat{\sigma}_C^z + \hat{\sigma}_A^z\hat{\sigma}_C^z + \hat{\sigma}_B^z\hat{\sigma}_C^z + (1-\Delta)\hat{\sigma}_A^z\hat{\sigma}_B^z. \quad (11)$$

This is a nonseparable three-body Ising-type interaction. Combining this Y junction with another three quantum wires connecting A with B, B with C, and C with A, this permits full programmability of all Ising interactions among the three qubits.

Since a spin flip in the ancilla leaving the low-energy subspace has an energy cost of $4(\Delta-2)J_Y$, the error rate of the Y-junction connector is exponentially suppressed and proportional to $e^{-4\beta J_Y(\Delta-2)}$ (β is the inverse temperature), provided that the temperature is much lower than the energy gap. In the presence of quantum fluctuations for example driven by $\hat{\sigma}_{A,B,C}^x$, the Y-junction connector is valid when assuming that the energy gap dominates over other energy scales.

In this context we note that a resolution of four-body Ising interactions into two-body interactions with an auxiliary spin has been discussed in Ref. [17]. More generally, an m-body interaction can be reduced to $(m-1)$-body interactions at the cost of introducing one ancilla using a Y junction because, with a Y junction, any three-body Ising interaction can be induced by two-body terms. This means that m-body interactions can be recursively reduced to two-body interactions eventually. The quantum wires mediating m-body interactions would then form a complex network, whose topology quickly becomes highly complex as m increases. For the quantum annealer construction, the complex network mediating m-body interactions can be further mapped with the qubit duplication scheme to the noncrossing architecture in three dimensions, as shown in Fig. 1. This implies that a locally coupled spin model on a 3D cubic lattice is sufficient to encode arbitrary all-to-all coupled Ising Hamiltonians.

C. Requirement on Ising coupling between duplicated qubits

In the 3D cubic quantum annealer [Eq. (8)], it is required to have $\hat{\sigma}_{ik}^z$ with the same i index ferromagnetically polarized in the ground state of H_P, because they represent the same logical qubit. In order to enforce this ferromagnetic polarization, it is adequate to choose

$$J_d < -K_{\max} D_{\max} \quad (12)$$

with $D_{\max}$ the maximal degree of G. With a finite maximal degree, the required coupling strength for J_d does not increase with qubit number. Even with all-to-all couplings, we suggest starting from a small number $r \equiv |J_d|/K_{\max} = 2$ and ramping it up until no defect is found in the duplicated qubits because the condition in Eq. (12) is unnecessary for typical instances, for the argument provided below. Only for the rare worst instances, it is required to set $r > D_{\max}$, which may compromise the physical computation speed by a factor of $1/r$ in the experimental implementation.

Here, we elaborate on the requirement on J_d to avoid defects in the duplicated qubits. With the condition in Eq. (12) satisfied, it is straightforward to show that the ground state of the 3D cubic quantum annealer has no defect in the duplicated qubits, because the energy penalty to have a defect induced by J_d is guaranteed to be larger than any possible energy gain. Here we argue that the defects in the duplicated qubits can still be sufficiently suppressed even if this condition is not satisfied. Setting $|J_d|/K_{\max} = r \geq 1$, the energy cost for a randomly distributed number of defects, N_D, is typically $4N_D|J_d|$ and the energy gain is smaller than $2N_D K_{\max}$, which means that such defects would not exist in the ground state. More of our concern is about the softer defects of spins flipping in continuous domains. Considering spin flips in a continuous domain, $\hat{\sigma}_{i_0,k_0}^z, \hat{\sigma}_{i_0,k_0+1}^z, \hat{\sigma}_{i_0,k_0+2}^z, \ldots, \hat{\sigma}_{i_0,k_0+l-1}^z$ with a domain size l, the energy cost for such defects is $4|J_d|$ if the domain is not at the boundary and is $2|J_d|$ otherwise. The maximal energy gain is $2lK_{\max}$, which is potentially larger than the energy cost. This would then cause errors in the 3D cubic quantum annealer as those defects are no longer energetically suppressed. However, the maximal energy gain is only reached for rare cases with all terms of $K_{i_0 i'} s_{i_0} s_{i'}$ $[(i_0+i') \bmod N = k_0, k_0+1, \ldots, k_0+l-1]$ being coherently positive in the actual ground state of the Hamiltonian in Eq. (1). Note that the links (ii') with $K_{ii'}s_i s_{i'} > 0$ in the ground state are frustrated. Such links do not exist in frustration-free models. In general, without fine tuning, the probability for that maximal energy gain to really happen should decay exponentially with l. With the choice $|J_d|/K_{\max} = r$, the probability for the 3D cubic quantum annealer to be erroneous is thus expected to decay exponentially with r. This argument is further confirmed with numerical simulations of Ising spin glass with all-to-all random couplings (Fig. 2), where the couplings $K_{ii'}$ are drawn from $[-1, 1]$ according to a uniform distribution. Given a ground state configuration, for each logical qubit index i_0, we define a maximal domain size $l_{\max}$ to be a maximal value of l that has all the links $(i_0 i')$ with $[(i_0+i') \bmod N = k_0, k_0+1, \ldots, k_0+l-1]$ being frustrated (i_0 and k_0 can be arbitrarily chosen). In Fig. 2, we show the probability distribution of $l_{\max}$ obtained from numerical simulations, and confirm that the probability distribution exhibits an exponential decay. The proposed 3D cubic architecture should thus provide a scalable quantum annealing Hamiltonian.

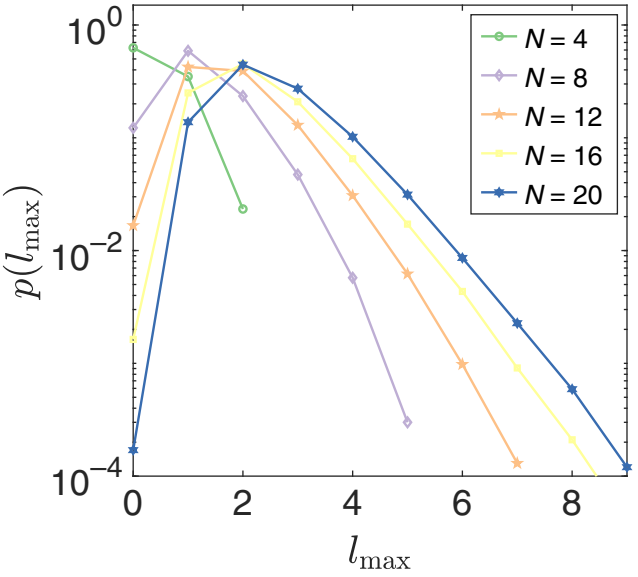

FIG. 2. The probability distribution of $l_{\max}$ in Ising spin glass ground states with random couplings. We simulate the Ising spin glass models with all-to-all random couplings with 4, 8, 12, 16, and 20 vertices. The random couplings are drawn from $[-1, 1]$ according to a uniform distribution. We obtain the ground state and calculate the value of $l_{\max}$ (see the main text). The statistics are taken over samples of 10^5 random problem instances. It is evident that the probability distribution $p(l_{\max})$ exhibits an exponential decay at large $l_{\max}$.

III. FINITE-TEMPERATURE EFFECT

Since the physical devices performing quantum annealing may not operate at absolute zero temperature, we describe finite-temperature effects in this section. In the following, we show that the scheme of quantum wire mediating long-range interaction provided in Sec. II has reasonable scalability even when taking into account thermal excitations. This is particularly crucial to optical lattice experimental implementation, discussed in Sec. V. Moreover, the scheme can be adapted to the construction of an annealer producing a finite-temperature ensemble.

A. Thermal defect causing error in the ferromagnetic quantum wire

Considering the finite-temperature effect, the thermally excited domain wall defects in the ancilla quantum wires may cause errors. We emphasize here that the error probability corresponds to having an odd number of domain walls in the Ising ferromagnetic quantum wire, because the effective coupling through a ferromagnetic wire with an even number of domain wall defects is equivalent to a wire in its ground state having no defect. In the presence of an even number of domain wall defects, the two spins at the ends are still ferromagnetically oriented as in the ground state, whereas their orientation is antiferromagnetic for an odd number of domain wall defects. In general, the ferromagnetic quantum wire with M ancilla that couples two distant qubits is described by the Hamiltonian $\hat{H}_J = J\sum_{j=0}^{M-2}\hat{\tau}_j^z\hat{\tau}_{j+1}^z$. The thermal ensemble of these ancilla is given by the density matrix operator $\hat{\rho} = \exp(-\beta\hat{H}_J)/\mathrm{Tr}[\exp(-\beta\hat{H}_J)]$ with β the inverse temperature. The Boltzmann constant is set as unity throughout.

The probability of having an odd number of domain wall defects (p_{err}) corresponds to the probability of the two end ancilla of the quantum wire being opposite. With a transfer matrix method [43], we obtain the error rate as

$$p_{\mathrm{err}} = \frac{[\lambda_+(J)]^{M-1} - [\lambda_-(J)]^{M-1}}{2[\lambda_+(J)]^{M-1}}, \tag{13}$$

where $\lambda_\pm(J) = e^{-\beta J} \pm e^{\beta J}$.

For an error rate below a certain threshold p_{th}, we let $p_{\mathrm{err}} < p_{\mathrm{th}}$, which leads to the temperature requirement $T < T_{\mathrm{th}}$, with temperature threshold

$$T_{\mathrm{th}} = 2|J|\left[\ln\frac{1+(1-2p_{\mathrm{th}})^{1/(M-1)}}{1-(1-2p_{\mathrm{th}})^{1/(M-1)}}\right]^{-1}. \tag{14}$$

Considering a small error rate threshold, we have $(1-2p_{\mathrm{th}})^{1/(M-1)} \approx 1 - 2p_{\mathrm{th}}/(M-1)$, and the temperature threshold takes the more illuminating form

$$T_{\mathrm{th}} \approx 2|J|\left[\ln\frac{M-1-p_{\mathrm{th}}}{p_{\mathrm{th}}}\right]^{-1}. \tag{15}$$

Therefore, the temperature threshold T_{th} decreases logarithmically with the length of the quantum wire M, or the distance of spins we are aiming to couple. We conclude that the proposed 3D cubic quantum annealing architecture is reasonably scalable even when taking into account the potential finite-temperature effect in the experimental implementation.

For choices of quantum wire lengths between 10 and 160, the numerical values of the error rate p_{err} and the temperature threshold T_{th} for $p_{\mathrm{th}} = 1/8$ are shown in Fig. 3. The temperature threshold is found to be of the order of several tenths of J.

B. Construction of a finite-temperature annealer

We further point out that the idea of using ferromagnetic quantum wires to couple distant logical qubits also applies to constructing an annealer that produces a finite-temperature ensemble. For each pair of spins (ii'), we have a ferromagnetic quantum wire with $M_{ii'}$ ancilla that couples to $\hat{\sigma}_i^z$ and $\hat{\sigma}_{i'}^z$, described by the Hamiltonian in Eq. (7). The thermal fluctuations are described by a density matrix operator $\hat{\rho}_{\mathrm{QWC}} \propto \exp(-\beta\hat{H}_{\mathrm{QWC},ii'})$. The induced couplings between $\hat{\sigma}_i^z$ and $\hat{\sigma}_{i'}^z$ are derived by tracing

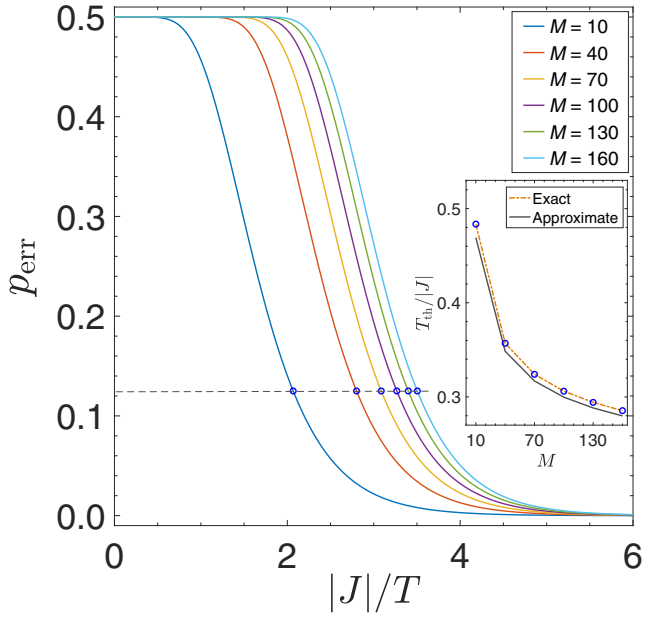

FIG. 3. The error rate ($p_{\rm err}$) in the ferromagnetic quantum wire at finite temperature (T). We choose a series of wire lengths, $M = 10, 40, 70, 100, 130, 160$. The gray dash line indicates a threshold probability of $p_{\rm th} = 1/8$. The inset shows the corresponding temperature threshold $T_{\rm th}$ with different M, calculated from the exact expression in Eq. (14) and the approximation in Eq. (15).

out the fluctuations of the ancilla, $\hat{\rho}_{\rm eff} = {\rm Tr}_{\rm ancilla}\left[\hat{\rho}_{\rm QWC}\right]$. To produce a thermal ensemble distribution determined by the Hamiltonian in Eq. (1), we require that $\hat{\rho}_{\rm eff} = Z_0 \exp\left(-\beta K_{ii'}\hat{\sigma}_i^z\hat{\sigma}_{i'}^z\right)$, where Z_0 is some arbitrary constant. With the transfer matrix method [43] we obtain

$$\exp(2\beta K) = \frac{\lambda_+(J_L)\lambda_+(J_R)[\lambda_+(J)]^{M-1} - \lambda_-(J_L)\lambda_-(J_R)[\lambda_-(J)]^{M-1}}{\lambda_+(J_L)\lambda_+(J_R)[\lambda_+(J)]^{M-1} + \lambda_-(J_L)\lambda_-(J_R)[\lambda_-(J)]^{M-1}}. \quad (16)$$

Here, the subscripts "ii'" labeling different quantum wires are suppressed in K, J_L, J_R, and M for ease of notation. At the zero-temperature limit, this result agrees with the domain wall construction that considers the ground state directly in Sec. II.

At finite temperature, Eq. (16) is satisfied by taking

$$J_{ii'} = -|K_{ii'}| - \ln[2(M_{ii'}-1)]/2\beta,$$
$$J_{L,ii'}/K_{ii'} = -J_{R,ii'}/|K_{ii'}| = -\frac{1}{2\beta|K_{ii'}|}\ln\frac{1-C_{ii'}}{1+C_{ii'}}, \quad (17)$$

where

$$C_{ii'} = \left(\frac{\lambda_-(-|K_{ii'}|)}{\lambda_+(-|K_{ii'}|)}\left[\frac{\lambda_+(J_{ii'})}{\lambda_-(J_{ii'})}\right]^{M_{ii'}-1}\right)^{1/2}.$$

This means that the required coupling strength in the quantum wire increases logarithmically with the length $M_{ii'}$, and that the magnitudes of J_L and J_R decrease monotonically with $M_{ii'}$ and β, having a lower bound, $|K_{ii'}|$. We thus conclude that the 3D cubic architecture is adaptable for finite-temperature annealing.

IV. NUMERICAL DEMONSTRATION

For demonstration, the proposed quantum annealing architecture is now applied to Max-Cut and prime factorization problems. In our protocol, it is required to have no defects in the duplicated logical qubits and in the quantum wire connectors. We thus simulate the quantum annealing process and check the number of defects in the duplicated qubits

$${\rm ND}_{\rm dup} = \frac{1}{2}\sum_i\sum_k[1 - \langle\hat{\sigma}_{ik}^z\hat{\sigma}_{i,k+1}^z\rangle] \quad (18)$$

and the number of defects in the quantum wires

$${\rm ND}_{\rm qw} = \frac{1}{2}\sum_{(ii')\in E}\sum_j[1 - \langle\hat{\tau}_{(ii'),j}^z\hat{\tau}_{(ii'),j+1}^z\rangle]. \quad (19)$$

In our simulation of the quantum dynamics, we set the Planck constant $\hbar$ as unity. We confirm that these defects are indeed suppressed in the quantum adiabatic evolution, solving both the Max-Cut and prime factorization problems. The simulation is carried out for very small system sizes for demonstration. The investigated problems could also be examples of demonstration experiments for small-scale quantum hardware.

A. Solving Max-Cut problems with the 3D cubic architecture

As a concrete demonstration, we simulate the performance of the 3D cubic quantum annealing architecture in solving Max-Cut problems. Given a graph G and an integer P, the Max-Cut problem is to determine whether there is bipartition of the graph that breaks at least P edges. This problem is NP complete. Finding the partition breaking the most edges is NP hard [4]. This problem arises in a broad range of applications, including financial portfolio optimization and social network analysis [4,38]. The fact that solving the Max-Cut problem on a classical computer is exponentially hard but its verification is easy makes it an ideal arena for quantum annealing to demonstrate the quantum advantage of application.

The spin glass Hamiltonian encoding the Max-Cut problem is that given in Eq. (1) with $K_{ii'}$ replaced with a constant positive value K to be set as 1 (the energy unit for the numerical results in Fig. 4) and the local fields $b_i = 0$. Following the standard quantum adiabatic computing, the initial state of the quantum annealer is set to

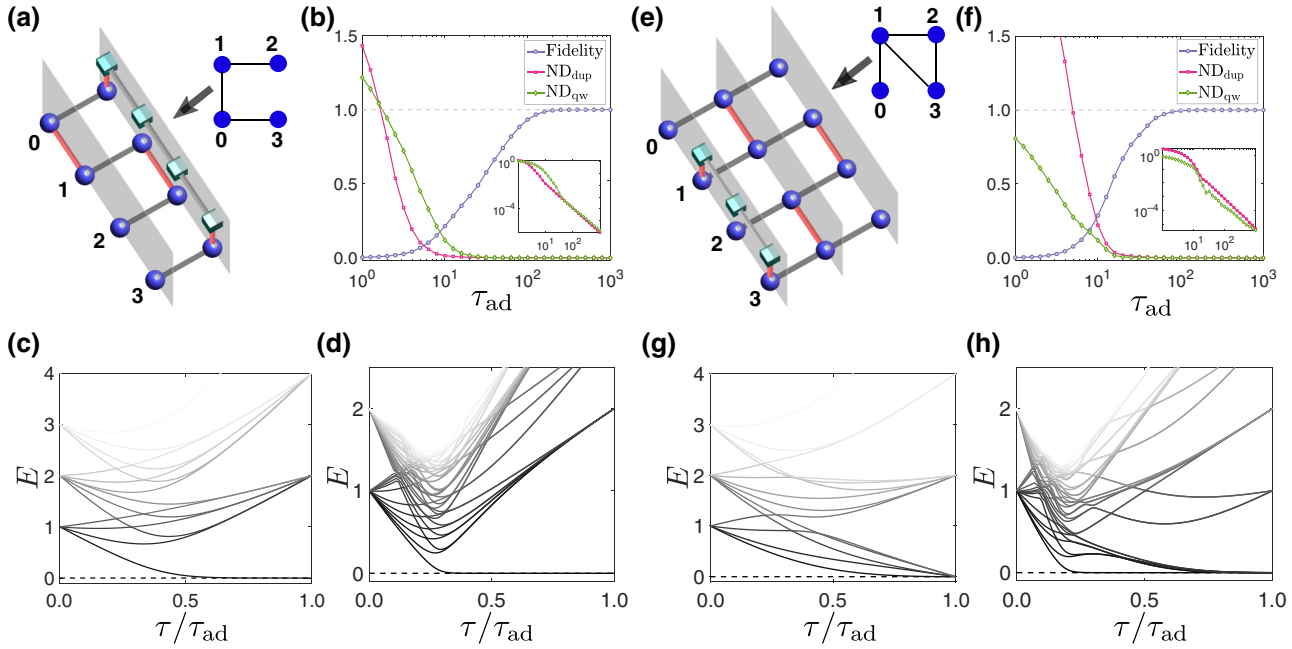

FIG. 4. Demonstration of the 3D cubic architecture for quantum annealing applied to Max-Cut problems. For the graphs shown at the top right of (a) and (e), we encode the Max-Cut problem of the graph in a spin glass model. The four logical qubits correspond to the four vertices in the graph. The corresponding 3D encoding architecture is shown in (a) and (e) with the unnecessary layers removed. The respective numerical performances are shown in (b) and (f), taking the local quantum annealing Hamiltonian in Eq. (8). Plots of the fidelity and the average numbers of defects in the duplication qubits, ND_{dup}, and in the connecting quantum wires, ND_{qw}, against the total adiabatic time τ_{ad} (see the main text). The insets show the monotonic decay behaviors of ND_{dup} and ND_{qw} at large τ_{ad}. For both cases, the quantum annealer reaches a fidelity of 50% around $\tau_{ad} = 20$. The defect numbers ND_{dup} and ND_{qw} drop to below 1% at about $\tau_{ad} = 30$, and decrease rapidly beyond that. The corresponding instantaneous eigenstate energy spectra for the lowest forty states are shown in (d) and (h). For comparison, the energy spectra with the direct nonlocal Hamiltonian in Eq. (2) are shown in (c) and (g). The energy spectra are all shifted with respect to the instantaneous ground state energy, and the dashed lines thus represent the ground state levels in (c), (d), (g), (h). The coupling in the Ising formulation of the Max-Cut problems is taken as an energy unit (see the main text). We choose the parameters $J_d = -1.1D_{max}$ and $J = -1.5$.

be the ground state of an initial Hamiltonian $\hat{H}_0$ [Eq. (8)]. The two example graphs are studied in Fig. 4. The expectation values of the numbers of defects in the duplicated qubits and in the quantum wire connectors with respect to the final quantum states, ND_{dup} and ND_{qw}, are shown in Fig. 4. The undesired defects are indeed greatly suppressed at a reasonable adiabatic evolution time. At long time, the time dependence of the defect numbers approaches a monotonic power-law decay, as expected from Kibble-Zurek theory [44]. For both studied graphs with [Figs. 4(c) and 4(d)] and without [Figs. 4(a) and 4(b)] loops, the quantum annealer reaches the correct solution of the Max-Cut problem with finite fidelity at a reasonable time cost. For comparison, we also calculate the instantaneous energy spectra for the direct nonlocal quantum annealing model in Eq. (2) and for the local quantum annealing in Eq. (8). For the studied Max-Cut problems, the energy gap above the ground state manifold of the latter is comparable to the former. Considering more difficult problems on larger graphs, eliminating the domain wall defects in the 3D local quantum annealer in the adiabatic quantum evolution would cause an increase in the time cost overhead, which we expect to scale polynomially with qubit number for the Kibble-Zurek scaling [44].

B. Factorization with the 3D cubic architecture

We further demonstrate that the 3D cubic quantum annealing architecture can be used to solve prime factorization, which has important implications in cryptography owing to the lack of efficient algorithms in classical computing. It has been shown that the problem of factorization can be solved by adiabatic quantum computing [10]. In our demonstration, we examine the factorization of $15 = p \times q$. With the binary representation $p = (z_0 1)_2$, $q = (z_2 z_1 1)_2$, finding the solution of (p, q) is equivalent to an optimization problem minimizing $(15 - p \times q)^2$. Through the binary representation, this optimization problem is encoded as solving the ground state of the Hamiltonian

$$H_p/\varepsilon = 32z_0z_1z_2 - 14z_0z_2 - 12z_0z_1 + 4z_1z_2 - 13z_0 - 13z_2 - 24z_1, \quad (20)$$

where ε is a rescaling factor, set as $1/32$ in our numerical simulation. The coupling strength of the three-body term $z_0z_1z_2$ then sets an energy unit. The z variables take boolean values, 0 and 1, and are related to Ising spins by $z_i = (s_i + 1)/2$. The three-body term is then reduced to a quadratic form using the Y-junction approach in Sec. II B, where we set the dimensionless parameter Δ in Eq. (10) as $\Delta = 4$. The resultant quadratic Ising spin glass model is further mapped to the local quantum annealing architecture [Eq. (8)], with the scheme developed in Sec. II. The corresponding 3D encoding architecture has 26 physical qubits [Fig. 5(a)] and is not compressible.

In Fig. 5(b) we show the performance of 3D local quantum annealing for prime factorization. With an adiabatic time $\tau_{\rm ad} > 20$, the defect excitations in the quantum wire connectors or the duplicated qubits become negligible. In the whole region of $\tau_{\rm ad}$ investigated, we find a monotonic increase in the fidelity, which reaches 10% at about $\tau_{\rm ad} = 100$. The instantaneous energy spectra for the direct quantum annealing of the nonlocal three-body model in Eq. (20) and for the local quantum annealing in Eq. (8) are shown in Figs. 5(c) and 5(d), respectively. The local quantum annealer has an energy gap above the ground state about one sixth of the nonlocal three-body model. This local encoding thus introduces an overhead in the time cost, considering the physics of the Landau-Zener transition [2,3]. In our numerics, we find that the limitation in the performance of 3D local quantum annealing is mainly from domain wall defects [Fig. 5(b)], whose number should follow a polynomial Kibble-Zurek scaling [44,45]. We thus expect that the overhead scales polynomially with qubit number, which is acceptable because an exponential quantum speedup with the quantum annealer is expected [10,11].

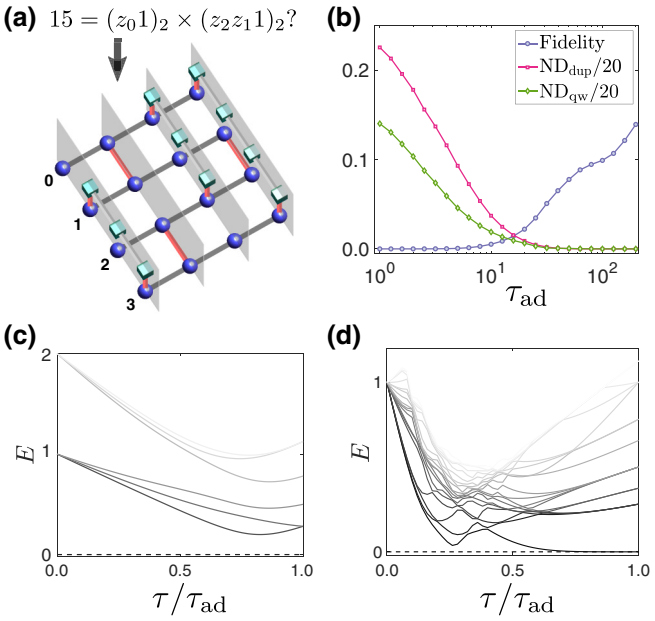

FIG. 5. Demonstration of the 3D cubic architecture for quantum annealing applied to prime factorization. A prime factorization of 15 is investigated. This problem is mapped to a spin glass model of four vertices with all-to-all couplings. (a) The 3D cubic quantum annealing architecture with 26 qubits. (b) Plots of the fidelity and the average numbers of defects in the duplication qubits, $\mathrm{ND_{dup}}$, and in the quantum wire connectors, $\mathrm{ND_{qw}}$, against the total adiabatic time $\tau_{\rm ad}$. The defect numbers $\mathrm{ND_{dup}}$ and $\mathrm{ND_{qw}}$ are rescaled for cosmetic reasons. Here we choose the parameters $J_d = -1.1D_{\max}K_{\max}$ and $J = -1.5K_{\max}$. The defect excitations become negligible for an adiabatic time $\tau_{\rm ad} > 20$. (d) The instantaneous eigenstate energy spectra of the local quantum annealing Hamiltonian in Eq. (8). We calculate the lowest twenty states. (c) The energy spectra for quantum annealing with the direct nonlocal three-body Hamiltonian [see Eq. (20)]. The energy spectra are shifted with respect to the instantaneous ground state energy, and the dashed lines thus represent the ground state levels in (c) and (d). The coupling strength of the three-body interaction is taken as an energy unit.

Remark 1: In solving the Max-Cut and prime factorization problems above, we chose a linear schedule in the adiabatic quantum computing [Eq. (8)], which may not have the best performance in terms of computation time. This time cost can be dramatically improved by optimizing the schedule [41,46], or adding counterdiabatic drivings [47–49].

V. EXPERIMENTAL CANDIDATES

For an experimental realization of the proposed quantum annealing architecture [see Eq. (8)], we focus on atomic systems for which 3D arrays including Ising quantum wires can be arranged with laser-created optical lattices [21] or tweezers [32]. In these systems, the dynamical manipulation of the geometry of qubits can be achieved by controlling lasers. Below we outline a physical implementation of the quantum annealer with superexchange in atomic Hubbard models and Rydberg p-wave dressing interactions for ultracold atoms confined in optical lattices.

A. Interaction design through atomic superexchange in an optical lattice

We consider atoms confined in a 3D optical lattice forming a Mott insulating state, with the atomic internal states encoding the qubits. With a far-detuned optical lattice, the familiar atomic superexchange is a Heisenberg interaction [50]. One approach to introduce Ising spin interactions as required in the quantum annealing model [see Eq. (8)] is to freeze the tunneling of one spin component, say spin $|\downarrow\rangle$, with a spin-dependent lattice potential, $V_\sigma(x) = (V_0 + \sigma V_1)\sum_{\nu=1,2,3}\sin^2(\pi x_\nu)$, where $\sigma = \pm$ represent two spin (or hyperfine) states of atoms confined in the lattice and $x_{1,2,3}$ three spatial coordinates [51–55]. The quantum dynamics is then characterized by the single particle tunneling of spin $|\uparrow\rangle$ atoms, $t_\uparrow$, the intraspecies Hubbard interaction, $U_{\uparrow\uparrow}$ ($U_{\downarrow\downarrow}$), between

spin up (down), and the interspecies interaction, $U_{\uparrow\downarrow}$. The virtual tunneling induced superexchange for bosonic atoms has a coupling strength $J_{\rm ex} = t_\uparrow^2/2U_{\uparrow\downarrow} - t_\uparrow^2/U_{\uparrow\uparrow}$ [50], which is ferromagnetic with $U_{\uparrow\downarrow} > U_{\uparrow\uparrow}/2$ and antiferromagnetic otherwise. The interactions in the lattice are related to the s-wave scattering lengths $a_{\sigma\sigma'}$ by $U_{\sigma\sigma'} = 4\pi(a_{\sigma\sigma'}\hbar^2/M)\int d^3x|w_\sigma(x)|^2|w_{\sigma'}(x)|^2$ with $w_\sigma(x)$ the Wannier function for the σ component, which depends on the local optical potential. Using Feshbach resonances [56], we tune the external magnetic field to adjust the scattering lengths such that $a_{\uparrow\downarrow} = a_{\uparrow\uparrow}/2$, and control the superexchange by manipulating the Wannier functions by adjusting the local optical potential with digital micromirror devices or related techniques [23,24,31]. The form of the demanded optical potential can be calculated using our recently developed algorithms that are highly efficient on a classical computer [27]. In this way, both ferromagnetic and antiferromagnetic couplings can be locally achieved.

For alkali atoms, a spin-dependent lattice for ground state atoms can be created by coupling to the D line P states with circularly polarized light [51,52]. This comes with a requirement that the fine structure splitting between $D1$ and $D2$ lines should be sufficiently large in order to have both strong enough spin dependence in the optical potential and a sufficiently suppressed spontaneous emission rate. We thus consider ^{39}K atoms whose $D1$-$D2$ splitting is about $2\pi \times 2$ THz. For K atoms, the superexchange at a lattice depth of 10 times the recoil energy is estimated to be $2\pi \times 30$ Hz, assuming that the Hubbard interaction is 10 times the single-particle tunneling and that the corresponding lattice-induced spontaneous emission rate is below 1/10 Hz. A temperature requirement is set by considering the thermally activated errors in the quantum wire connectors. For example, an error rate below 1% requires the temperature to be below $2\pi \times 10$ Hz for a quantum wire of length $M = 100$, as obtained from Eq. (13). We caution here that the potential challenge with alkali atoms could arise from the spin-dependent lattice-induced heating, which should be investigated in experimental studies.

For alkaline earth atoms, the spin can be encoded in long lived clock states [54,57]. A spin-dependent optical lattice realizing the Ising interaction can then be implemented due to the different ac polarizabilities of the ground and excited atomic states. In this system, the Hubbard interaction is controllable with an orbital Feshbach resonance [58,59]. With fermionic ^{87}Sr atoms, an Ising superexchange interaction can be made to the order $2\pi \times 10$ Hz [57], which can be tuned to be either ferromagnetic or antiferromagnetic using the spin-orbit coupling techniques achieved in present experiments [60]. The experimental system has a quantum coherence time of about 10 s [61], for which the computation problems studied in Sec. IV can be experimentally tested. For larger-size computation problems, it is helpful to consider performing optimization over the Hamiltonian evolution path [41,46–49] or adopting the iterative quantum annealing approach [62].

Our 3D cubic encoding protocol implies that a cubic optical lattice with a spatially controllable potential would support programmable quantum annealing, although a 3D holographic control over the optical potential still requires further technological developments.

B. Rydberg dressing scheme

Ising spin interactions in the quantum annealing architecture can also be implemented with laser-excited Rydberg atoms stored in tweezer arrays [32] or optical lattices [21]. In addition, a proper choice of the Rydberg state allows an anisotropic, directional Ising interaction that allows us to minimize the cross talk between the quantum wires. In the quantum annealing architecture [Fig. 1(c)], the required Ising interactions are highly anisotropic—quantum wires in different k layers must be decoupled, and most of the duplicated logical qubits are decoupled along the i direction. To fulfil the anisotropy, it is natural to consider Rydberg p-wave interaction [63].

Specifically, we consider the hyperfine states $|5^2S_{1/2}, F = 2, m_F = 0\rangle$ and $|5^2S_{1/2}, F = 1, m_F = 0\rangle$ of ^{87}Rb atoms for qubit encoding as spin $|\uparrow\rangle$ and $|\downarrow\rangle$, respectively. We consider a Rydberg dressing scheme [28,29] with the $|\uparrow\rangle$ state selectively dressed with a Rydberg p state via a circularly polarized laser light to introduce interactions between nearest neighboring atoms in $|\uparrow\rangle$, realizing the Ising couplings in Eq. (8). The local fields are controllable by adjusting the laser detuning. In this scheme, we use two p states, $|r_\bullet\rangle = |n^2P_{3/2}, m = 3/2\rangle_i$ and $|r_\blacksquare\rangle = |n^2P_{3/2}, m = 3/2\rangle_k$, where i and k indicate the quantization axes (see Fig. 6) [63]. Since the interaction programmability requires local controllability of Rydberg dressing, it is experimentally more convenient to confine cold atoms in a lattice with a large lattice constant, for example about a few microns, as used to perform single qubit gates on individual atoms [31]. The angle dependence of van der Waals interactions between atoms dressed with $|r_\bullet\rangle$ and with $|r_\blacksquare\rangle$, $V_{\bullet\bullet}$ and $V_{\blacksquare\blacksquare}$, respectively, is given in Ref. [63]. The key feature in these interactions as is relevant to our quantum annealer implementation here is their anisotropy—$V_{\bullet\bullet}$ and $V_{\blacksquare\blacksquare}$ vanish along the i and k directions, respectively. The mixed interaction $V_{\bullet\blacksquare}$ between the two Rydberg p states takes the form

$$V_{\bullet\blacksquare} \sim \frac{n^{11}}{r^6} A(\theta, \phi). \tag{21}$$

Here, the spherical coordinates (r, θ, ϕ) denote the relative position between two atoms, where the north pole corresponds to the $+i$ direction and the azimuthal angle measures the direction in the k-h plane (Fig. 6). The angular part of the mixed interaction $V_{\bullet\blacksquare}$ is $A(\theta, \phi) = \frac{1}{576}[37 - 12\cos 2\theta - 9\cos 4\theta + 48\sin 2\theta\cos\phi + 12(1 + 3\cos 2\theta)$

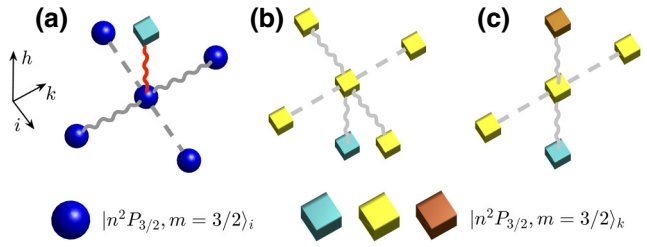

FIG. 6. Illustration of Rydberg p-wave building blocks for implementation of the 3D cubic quantum annealing architecture. The atoms at the sites of spheres and cubes are dressed by the Rydberg states $|n^2P_{3/2}, m = 3/2\rangle_i$ and $|n^2P_{3/2}, m = 3/2\rangle_k$, respectively, with the subscripts i and k denoting the quantization axes. Solid (dashed) lines indicate the presence (absence) of couplings between the two Rydberg dressed atoms. For the angular dependence of the Rydberg p-wave interaction [Eq. (21)], in the horizontal i-k plane the duplicated logical qubits (ancilla) only couple to each other along the k (i) direction as shown in (a),(b). Along the vertical h direction, both the duplicated logical qubits and the ancilla interact with their neighbors, as shown in (a)–(c). The red link representing a programmable Ising coupling is realized by the mixed interaction between the two different Rydberg states. This coupling orientation corresponds to $(\theta = \pi/2, \phi = \pi/2)$ in the angular dependence of the mixed interaction.

$\sin^2\theta\cos 2\phi]$, which vanishes at $(\theta = -1/2\arcsin(2/3), \phi = 0)$, and is about two thirds of its maximal value at $(\theta = \pi/2, \phi = \pi/2)$.

The atoms in the lattice representing the duplicated logical qubits ["spheres" in Fig. 1(c)] and the ancilla ("cubes") are dressed with Rydberg p states $|r_\bullet\rangle$ and $|r_\blacksquare\rangle$, respectively. The strong angular dependence of the Rydberg p-wave interaction allows for engineering the required interactions in Eq. (8). As shown in Fig. 6, the duplicated logical qubits are coupled along the k axis, but are decoupled along the i axis. Likewise, the ancilla are coupled only within each k layer as required. The interactions between the duplicated logical qubits and the ancilla, as required to be programmable to encode the original Ising spin couplings [see Eq. (5)], are realized by the mixed interaction $V_{\bullet\blacksquare}$ in Eq. (21). The programmability is achieved by considering spatial-resolved control over the Rydberg dressing laser detuning [28,29]. With the Condon radius of Rydberg dressing set close to the lattice constant, next neighboring interactions are one-to-two orders of magnitude smaller than the nearest neighbor due to the $1/r^6$ decay of the van der Waals interaction [34], which are thus negligible.

We remark here that the 3D quantum annealing architecture should be slightly adjusted for Rydberg implementation in order to suppress the unwanted couplings, for example the couplings between two quantum wire connectors with heights that differ by 1. The direct couplings at height $h = 0$ should be replaced by introducing an additional quantum wire connector at height $h = 1$. Each k layer that contains the quantum wires labeled (ii') with $\underline{i + i'} = k$ is split into two, according to the height of the quantum wire being even or odd.

With a proper choice of the detuning and Rabi frequency in the Rydberg dressing, an interaction strength of the order of several kilohertz can be obtained [63], which leads to a computation time of tens of milliseconds for the problems studied in Sec. IV. The computation time can be improved further by schedule optimization [41,46], or by adding counterdiabatic driving [47–49]. Besides Rydberg dressing, an alternative approach is to encode the qubit with one atomic ground state and one Rydberg state [32], which has a shorter lifetime but stronger interaction. Further considering Förster resonances controllable via external electric or microwave fields [64], the interaction strength and the angular dependence would introduce a larger degree of tunability, making the Rydberg implementation a rather promising platform for programmable quantum annealing. All required ingredients in the Rydberg-based quantum annealing architecture are accessible with near-term quantum technology.

Another experimental candidate for implementing the 3D quantum annealing architecture are polar molecules. By confining polar molecules in an array with optical tweezer techniques, the neighboring interactions can be made of the order of kilohertz and are locally controllable [65,66]. The natural long-range anisotropic interactions with polar molecules realize the fixed couplings in the quantum wire connectors and the long-range part of the interaction is expected to make the connectors more stiff, further suppressing defect excitations in the quantum wire. The programmable couplings can be achieved with ac-Stark shift of tightly focused laser beams [65].

VI. DISCUSSION AND OUTLOOK

We have proposed Ising quantum wires to build long-range connectivity for programmable quantum annealing, by which a local quantum annealing architecture is developed. This setup can be embedded in a regular cubic lattice and only contains local fields and nearest-neighbor couplings. This can be implemented in experiments comprising a system of ground state atoms in a spin-dependent optical lattice, or Rydberg p-wave dressed atoms confined in a large-spacing optical lattice or tweezer arrays. The quantum annealing architecture has reasonable robustness against finite-temperature effects, and has good protection against readout errors from the logical qubit duplication. Our theory implies large-scale quantum annealing is accessible to near-term optical lattice techniques. We have demonstrated how the theory applies to Max-Cut and prime factorization problems by simulating relatively small size problems on a classical computer. The present scheme of Ising quantum wires connecting spins

in the quantum annealing problem can also be implemented in solid-state architectures, including superconducting devices [39] and quantum dots [40], the main experimental challenge being the development of multilayered chips to represent the connecting wires. While the long-term vision is an experimental realization of the 3D cubic architecture towards a programmable quantum annealer with all-to-all connectivity, we note that an experimental roadmap will first of all have to focus on basis building blocks like demonstration of m-port quantum wires and Ising interactions, which also provide interesting opportunities in quantum simulation of exotic spin models.

ACKNOWLEDGMENT

We acknowledge helpful discussions with Yu-Ao Chen, Saijun Wu, Han-Ning Dai, and Xingcan Yao. This work is supported by the National Natural Science Foundation of China (Grants No. 11934002 and No. 11774067), the National Program on Key Basic Research Project of China (Grant No. 2017YFA0304204), and the Shanghai Municipal Science and Technology Major Project (Grant No. 2019SHZDZX01). X.Q. acknowledges support from the National Postdoctoral Program for Innovative Talents of China under Grant No. BX20190083. Work at Innsbruck is supported by the European Union program Horizon 2020 under Grant Agreement No. 817482 (PASQuanS).

[1] E. Farhi, J. Goldstone, S. Gutmann, J. Lapan, A. Lundgren, and D. Preda, A quantum adiabatic evolution algorithm applied to random instances of an NP-Complete problem, Science **292**, 472 (2001).
[2] A. Das and B. K. Chakrabarti, Colloquium: Quantum annealing and analog quantum computation, Rev. Mod. Phys. **80**, 1061 (2008).
[3] T. Albash and D. A. Lidar, Adiabatic quantum computation, Rev. Mod. Phys. **90**, 015002 (2018).
[4] A. Lucas, Ising formulations of many NP problems, Front. Phys. **2**, 5 (2014).
[5] T. Jörg, F. Krzakala, J. Kurchan, and A. C. Maggs, Simple Glass Models and Their Quantum Annealing, Phys. Rev. Lett. **101**, 147204 (2008).
[6] N. G. Dickson and M. H. S. Amin, Does Adiabatic Quantum Optimization Fail for NP-Complete Problems?, Phys. Rev. Lett. **106**, 050502 (2011).
[7] B. Altshuler, H. Krovi, and J. Roland, Anderson localization makes adiabatic quantum optimization fail, Proc. Natl. Acad. Sci. **107**, 12446 (2010).
[8] H. G. Katzgraber, F. Hamze, and R. S. Andrist, Glassy chimeras could be blind to quantum speedup: Designing better benchmarks for quantum annealing machines, Phys. Rev. X **4**, 021008 (2014).
[9] T. F. Ronnow, Z. Wang, J. Job, S. Boixo, S. V. Isakov, D. Wecker, J. M. Martinis, D. A. Lidar, and M. Troyer, Defining and detecting quantum speedup, Science **345**, 420 (2014).
[10] X. Peng, Z. Liao, N. Xu, G. Qin, X. Zhou, D. Suter, and J. Du, Quantum Adiabatic Algorithm for Factorization and Its Experimental Implementation, Phys. Rev. Lett. **101**, 220405 (2008).
[11] S. Jiang, K. A. Britt, A. J. McCaskey, T. S. Humble, and S. Kais, Quantum annealing for prime factorization, Sci. Rep. **8**, 17667 (2018).
[12] L. Zhou, S.-T. Wang, S. Choi, H. Pichler, and M. D. Lukin, Quantum Approximate Optimization Algorithm: Performance, Mechanism, and Implementation on Near-Term Devices, Phys. Rev. X **10**, 021067 (2020).
[13] J. King, S. Yarkoni, J. Raymond, I. Ozfidan, A. D. King, M. M. Nevisi, J. P. Hilton, and C. C. McGeoch, Quantum annealing amid local ruggedness and global frustration, arXiv:1701.04579 [quant-ph] (2017).
[14] S. Boixo, T. F. Rønnow, S. V. Isakov, Z. Wang, D. Wecker, D. A. Lidar, J. M. Martinis, and M. Troyer, Evidence for quantum annealing with more than one hundred qubits, Nat. Phys. **10**, 218 (2014).
[15] W. Lechner, P. Hauke, and P. Zoller, A quantum annealing architecture with all-to-all connectivity from local interactions, Sci. Adv. **1**, e1500838 (2015).
[16] A. Rocchetto, S. C. Benjamin, and Y. Li, Stabilizers as a design tool for new forms of the Lechner-Hauke-Zoller annealer, Sci. Adv. **2**, e1601246 (2016).
[17] A. W. Glaetzle, R. M. W. van Bijnen, P. Zoller, and W. Lechner, A coherent quantum annealer with Rydberg atoms, Nat. Commun. **8**, 15813 (2017).
[18] H. Pichler, S.-T. Wang, L. Zhou, S. Choi, and M. D. Lukin, Computational complexity of the rydberg blockade in two dimensions, arXiv:1809.04954 [quant-ph] (2018).
[19] E. Altman *et al.*, Quantum simulators: Architectures and opportunities, arXiv:1912.06938 [quant-ph] (2019).
[20] Y. Alexeev *et al.*, Quantum computer systems for scientific discovery, arXiv:1912.07577 [quant-ph] (2019).
[21] C. Gross and I. Bloch, Quantum simulations with ultracold atoms in optical lattices, Science **357**, 995 (2017).
[22] W. Yi, A. J. Daley, G. Pupillo, and P. Zoller, State-dependent, addressable subwavelength lattices with cold atoms, New J. Phys. **10**, 073015 (2008).
[23] G. Gauthier, I. Lenton, N. M. Parry, M. Baker, M. Davis, H. Rubinsztein-Dunlop, and T. Neely, Direct imaging of a digital-micromirror device for configurable microscopic optical potentials, Optica **3**, 1136 (2016).
[24] A. Mazurenko, C. S. Chiu, G. Ji, M. F. Parsons, M. Kanász-Nagy, R. Schmidt, F. Grusdt, E. Demler, D. Greif, and M. Greiner, A cold-atom Fermi–Hubbard antiferromagnet, Nature **545**, 462 (2017).
[25] M. McDonald, J. Trisnadi, K.-X. Yao, and C. Chin, Superresolution Microscopy of Cold Atoms in an Optical Lattice, Phys. Rev. X **9**, 021001 (2019).
[26] S. Subhankar, Y. Wang, T.-C. Tsui, S. L. Rolston, and J. V. Porto, Nanoscale Atomic Density Microscopy, Phys. Rev. X **9**, 021002 (2019).
[27] X. Qiu, J. Zou, X. Qi, and X. Li, Precise programmable quantum simulations with optical lattices, Npj Quantum Inf. **6**, 1 (2020).
[28] J. Honer, H. Weimer, T. Pfau, and H. P. Büchler, Collective Many-Body Interaction in Rydberg Dressed Atoms, Phys. Rev. Lett. **105**, 160404 (2010).

[29] G. Pupillo, A. Micheli, M. Boninsegni, I. Lesanovsky, and P. Zoller, Strongly Correlated Gases of Rydberg-Dressed Atoms: Quantum and Classical Dynamics, Phys. Rev. Lett. **104**, 223002 (2010).

[30] M. Viteau, M. G. Bason, J. Radogostowicz, N. Malossi, D. Ciampini, O. Morsch, and E. Arimondo, Rydberg Excitations in Bose-Einstein Condensates in Quasi-One-Dimensional Potentials and Optical Lattices, Phys. Rev. Lett. **107**, 060402 (2011).

[31] Y. Wang, A. Kumar, T.-Y. Wu, and D. S. Weiss, Single-qubit gates based on targeted phase shifts in a 3D neutral atom array, Science **352**, 1562 (2016).

[32] A. Browaeys and T. Lahaye, Many-body physics with individually controlled Rydberg atoms, Nat. Phys. **16**, 132 (2020).

[33] L.-M. Duan and C. Monroe, Colloquium: Quantum networks with trapped ions, Rev. Mod. Phys. **82**, 1209 (2010).

[34] M. Saffman, T. G. Walker, and K. Mølmer, Quantum information with Rydberg atoms, Rev. Mod. Phys. **82**, 2313 (2010).

[35] S. Weinberg, *The Quantum Theory of Fields* (Cambridge University Press, Cambridge, 1995), Vol. I.

[36] B. Clark, C. Colbourn, and D. Johnson, Unit disk graphs, Discrete Math. **86**, 165 (1990).

[37] J. M. Crawford and L. D. Auton, in *Proceedings of the 11th National Conference on Artificial Intelligence* (AAAI, Menlo Park, 1993), Vol. 93, p. 21.

[38] A.-L. Barabási and R. Albert, Emergence of scaling in random networks, Science **286**, 509 (1999).

[39] M. Kjaergaard, M. E. Schwartz, J. Braumüller, P. Krantz, J. I.-J. Wang, S. Gustavsson, and W. D. Oliver, Superconducting qubits: Current state of play, Annu. Rev. Condens. Matter Phys. **11**, 369 (2020).

[40] F. A. Zwanenburg, A. S. Dzurak, A. Morello, M. Y. Simmons, L. C. L. Hollenberg, G. Klimeck, S. Rogge, S. N. Coppersmith, and M. A. Eriksson, Silicon quantum electronics, Rev. Mod. Phys. **85**, 961 (2013).

[41] J. Lin, Z. Y. Lai, and X. Li, Quantum adiabatic algorithm design using reinforcement learning, Phys. Rev. A **101**, 052327 (2020).

[42] E. Boros and P. L. Hammer, Pseudo-boolean optimization, Discrete Appl. Math. **123**, 155 (2002).

[43] A. Altland and B. D. Simons, *Condensed Matter Field Theory* (Cambridge University Press, New York, 2010).

[44] T. W. B. Kibble, Topology of cosmic domains and strings, J. Phys. A: Math. Gen. **9**, 1387 (1976).

[45] W. H. Zurek, Cosmological experiments in superfluid helium?, Nature **317**, 505 (1985).

[46] Y.-Q. Chen, Y. Chen, C.-K. Lee, S. Zhang, and C.-Y. Hsieh, Optimizing quantum annealing schedules: From monte carlo tree search to quantumzero, arXiv:2004.02836 [quant-ph] (2020).

[47] M. Demirplak and S. A. Rice, Adiabatic population transfer with control fields, J. Phys. Chem. A **107**, 9937 (2003).

[48] M. V. Berry, Transitionless quantum driving, J. Phys. A: Math. Theor. **42**, 365303 (2009).

[49] M. Kolodrubetz, D. Sels, P. Mehta, and A. Polkovnikov, Geometry and non-adiabatic response in quantum and classical systems, Phys. Rep. **697**, 1 (2017).

[50] L.-M. Duan, E. Demler, and M. D. Lukin, Controlling Spin Exchange Interactions of Ultracold Atoms in Optical Lattices, Phys. Rev. Lett. **91**, 090402 (2003).

[51] D. Jaksch, H.-J. Briegel, J. I. Cirac, C. W. Gardiner, and P. Zoller, Entanglement of Atoms Via Cold Controlled Collisions, Phys. Rev. Lett. **82**, 1975 (1999).

[52] W. V. Liu, F. Wilczek, and P. Zoller, Spin-dependent Hubbard model and a quantum phase transition in cold atoms, Phys. Rev. A **70**, 033603 (2004).

[53] P. J. Lee, M. Anderlini, B. L. Brown, J. Sebby-Strabley, W. D. Phillips, and J. V. Porto, Sublattice Addressing and Spin-Dependent Motion of Atoms in a Double-Well Lattice, Phys. Rev. Lett. **99**, 020402 (2007).

[54] A. J. Daley, M. M. Boyd, J. Ye, and P. Zoller, Quantum Computing with Alkaline-Earth-Metal Atoms, Phys. Rev. Lett. **101**, 170504 (2008).

[55] H.-N. Dai, B. Yang, A. Reingruber, H. Sun, X.-F. Xu, Y.-A. Chen, Z.-S. Yuan, and J.-W. Pan, Four-body ring-exchange interactions and anyonic statistics within a minimal toric-code Hamiltonian, Nat. Phys. **13**, 1195 (2017).

[56] C. Chin, R. Grimm, P. Julienne, and E. Tiesinga, Feshbach resonances in ultracold gases, Rev. Mod. Phys. **82**, 1225 (2010).

[57] M. Mamaev, R. Blatt, J. Ye, and A. M. Rey, Cluster State Generation with Spin-Orbit Coupled fermionic Atoms in Optical Lattices, Phys. Rev. Lett. **122**, 160402 (2019).

[58] R. Zhang, Y. Cheng, H. Zhai, and P. Zhang, Orbital Feshbach Resonance in Alkali-Earth Atoms, Phys. Rev. Lett. **115**, 135301 (2015).

[59] M. Höfer, L. Riegger, F. Scazza, C. Hofrichter, D. R. Fernandes, M. M. Parish, J. Levinsen, I. Bloch, and S. Fölling, Observation of an Orbital Interaction-Induced Feshbach Resonance in ^{173}Yb, Phys. Rev. Lett. **115**, 265302 (2015).

[60] S. Kolkowitz, S. Bromley, T. Bothwell, M. Wall, G. Marti, A. Koller, X. Zhang, A. Rey, and J. Ye, Spin–orbit-coupled fermions in an optical lattice clock, Nature **542**, 66 (2017).

[61] A. Goban, R. B. Hutson, G. E. Marti, S. L. Campbell, M. A. Perlin, P. S. Julienne, J. P. D'Incao, A. M. Rey, and J. Ye, Emergence of multi-body interactions in a fermionic lattice clock, Nature **563**, 369 (2018).

[62] T. Graß, Quantum Annealing with Longitudinal Bias Fields, Phys. Rev. Lett. **123**, 120501 (2019).

[63] A. W. Glaetzle, M. Dalmonte, R. Nath, I. Rousochatzakis, R. Moessner, and P. Zoller, Quantum Spin-Ice and Dimer Models with Rydberg Atoms, Phys. Rev. X **4**, 041037 (2014).

[64] S. Weber, C. Tresp, H. Menke, A. Urvoy, O. Firstenberg, H. P. Büchler, and S. Hofferberth, Calculation of Rydberg interaction potentials, J. Phys. B: At., Mol. Opt. Phys. **50**, 133001 (2017).

[65] L. Anderegg, L. W. Cheuk, Y. Bao, S. Burchesky, W. Ketterle, K.-K. Ni, and J. M. Doyle, An optical tweezer array of ultracold molecules, Science **365**, 1156 (2019).

[66] P. Yu, L. W. Cheuk, I. Kozyryev, and J. M. Doyle, A scalable quantum computing platform using symmetric-top molecules, New J. Phys. **21**, 093049 (2019).